Cerebral Cortex, 2020;00: 1–16

doi: 10.1093/cercor/bhaa233
Original Article

ORIGINAL ARTICLE

3D Ultrastructural Study of Synapses in the Human Entorhinal Cortex

M. Domínguez-Álvaro[1], M. Montero-Crespo[1,2], L. Blazquez-Llorca[1,3], J. DeFelipe[1,2,4] and L. Alonso-Nanclares[1,2,4]

[1]Laboratorio Cajal de Circuitos Corticales, Centro de Tecnología Biomédica, Universidad Politécnica de Madrid. Pozuelo de Alarcón, Madrid 28223, Spain, [2]Instituto Cajal, Consejo Superior de Investigaciones Científicas (CSIC), Avda. Doctor Arce, 37 Madrid, 28002, Spain, [3]Depto. Psicobiología, Facultad de Psicología, Universidad Nacional de Educación a Distancia (UNED), c/Juan del Rosal, 10, Madrid 28040, Spain and [4]Centro de Investigación Biomédica en Red sobre Enfermedades Neurodegenerativas (CIBERNED), c/Valderrebollo, 5, Madrid 28031, Spain

Address correspondence to L. Alonso-Nanclares, Laboratorio Cajal de Circuitos Corticales, Centro de Tecnología Biomédica, Universidad Politécnica de Madrid. Pozuelo de Alarcón, Madrid 28223, Spain and Instituto Cajal, Consejo Superior de Investigaciones Científicas (CSIC), Avda. Doctor Arce, 37, Madrid 28002, Spain. Email: aidil@cajal.csic.es.

Abstract

The entorhinal cortex (EC) is a brain region that has been shown to be essential for memory functions and spatial navigation. However, detailed three-dimensional (3D) synaptic morphology analysis and identification of postsynaptic targets at the ultrastructural level have not been performed before in the human EC. In the present study, we used Focused Ion Beam/Scanning Electron Microscopy to perform a 3D analysis of the synapses in the neuropil of medial EC in layers II and III from human brain autopsies. Specifically, we studied synaptic structural parameters of 3561 synapses, which were fully reconstructed in 3D. We analyzed the synaptic density, 3D spatial distribution, and type (excitatory and inhibitory), as well as the shape and size of each synaptic junction. Moreover, the postsynaptic targets of synapses could be clearly determined. The present work constitutes a detailed description of the synaptic organization of the human EC, which is a necessary step to better understand the functional organization of this region in both health and disease.

Key words: cerebral cortex, electron microscopy, FIB-SEM, neuropil, synaptology

Introduction

The entorhinal cortex (EC) is a brain region, which is located on the anterior part of the medial temporal lobe and which has been shown to be essential for memory functions and spatial navigation (reviewed in Schultz et al. 2015). A number of neurodegenerative conditions, including Alzheimer's disease, have been related to alterations in the EC (Braak and Braak 1992). In particular, cognitive deficits have been linked to alterations in the upper layers of EC (Van Hoesen et al. 1991; Gomez-Isla et al. 1996).

Data regarding connections from human EC are mostly inferred from rodents and non-human primates. The EC itself is the origin of the perforant pathway (from layers II and III), which provides the largest input source to the hippocampal formation. Specifically, the EC layer II neurons project primarily to the dentate gyrus (DG) and CA3, whereas EC layer III neurons send their axons to the subiculum (SUB) and CA1 (Kondo et al. 2009; Insausti and Amaral 2012). These direct projections of the EC are essential for the proper functioning of the hippocampal formation. The classic trisynaptic circuit (layer II → DG → CA3 → CA1) seems to be related to the acquisition

of new memories, whereas the pathway between EC and CA1 neurons (monosynaptic) is thought to contribute to the strength of previously established memories (Cohen and Squire 1980). Once the information has passed through the hippocampus, it returns to the neurons of the deep layers of the EC (V/VI). These neurons project to the upper layers of the EC itself, sending the information back to the cortical association areas. In addition to establishing reciprocal connections with different association cortices, the EC establishes interconnections with subcortical structures such as the amygdala, septal nuclei or the thalamus, as well as with adjacent regions such as perirhinal cortex, parahippocampal cortex or insular cortex (Van Hoesen et al. 1991; Braak and Braak 1992; Duvernoy 2005; DeFelipe et al. 2007; Insausti and Amaral 2012). In this way, the EC acts as a gateway for sensory information to the hippocampal formation, also filtering the return of sensory information processed by the hippocampus to the different association areas. Thus, in terms of connections, the EC can be considered as an interface between the hippocampal formation and a large variety of association and limbic cortices (Solodkin and Van Hoesen 1996; Lavenex and Amaral 2000).

Furthermore, the EC is not a homogeneous region, as it presents a number of subfields along with its extent (reviewed in Schultz et al. 2015; Insausti et al. 2017). Whereas the medial EC interconnects with the parahippocampal cortex, the lateral EC interconnects with the perirhinal cortex. Both medial and lateral EC are connected to the hippocampal formation, including DG, CAs, and SUB (reviewed in Schultz et al. 2015). Thus, mapping the EC connectivity may contribute to the understanding of its structural design. One possible approach to decipher EC connectivity is its analysis at the ultrastructural level, using electron microscopy (EM), to map true synaptic contacts (or synapses).

In the present study, we used Focused Ion Beam/Scanning Electron Microscopy (FIB/SEM) to perform a three-dimensional (3D) analysis of the synapses of medial EC in layers II and III from "normal" human brain autopsies. FIB/SEM has already yielded excellent results in human brain samples (Domínguez-Álvaro et al. 2018, 2019; Montero-Crespo et al. 2020). Specifically, we studied a variety of synaptic structural parameters of 3561 synapses, which were fully reconstructed in 3D. In particular, we analyzed the synaptic density, 3D spatial distribution, and type (asymmetric [AS] and symmetric [SS], corresponding to excitatory and inhibitory synapses, respectively), as well as the shape and size of each synaptic junction. Moreover, the postsynaptic targets of 2768 synapses were clearly determined. These detailed morphological data provide quantitative information on the synaptology of this particular brain region and its layers. Thus, data from the present work constitute a detailed description of the synaptic organization in superficial layers of the human EC, which is a necessary step to better understand its functional organization in both health and disease.

Materials and Methods

Tissue Preparation

Human brain tissue was obtained from autopsies (with short postmortem delays of less than 3.5 h) from 4 male subjects with no recorded neurological or psychiatric alterations (supplied by Instituto de Neuropatología del IDIBELL,Hospital Universitario de Bellvitge, Barcelona, Spain; Unidad Asociada Neuromax, Laboratorio de Neuroanatomía Humana, Facultad de Medicina, Universidad de Castilla-La Mancha, Albacete, Spain; and the Laboratorio Cajal de Circuitos Corticales UPM-CSIC, Madrid, Spain) (Table 1). The sampling procedure was approved by the Institutional Ethical Committee. Tissue from some of these human brains has been used in previous studies (Domínguez-Álvaro et al. 2018, 2019; Montero-Crespo et al. 2020). Brain tissue samples were obtained following the guidelines and approval of the Institutional Ethical Committee from all involved institutions.

Upon removal, brain tissue was fixed in cold 4% paraformaldehyde (Sigma-Aldrich, St Louis, MO, USA) in 0.1 M sodium phosphate buffer (PB; Panreac, 131 965, Spain), pH 7.4, for 24-48 h. After fixation, the tissue was washed in PB and sectioned coronally in a vibratome (150 µm thickness; Vibratome Sectioning System, VT1200S Vibratome, Leica Biosystems, Germany). Sections containing EC were selected and processed for Nissl-staining and immunocytochemistry to determine cytoarchitecture (Fig. 1).

Immunohistochemistry

Selected sections were first rinsed in PB 0.1 M, pretreated in 2% H_2O_2 for 30 minutes to remove endogenous peroxidase activity, and then incubated for 1 h at room temperature in a solution of 3% normal horse serum (Vector Laboratories Inc., Burlingame, CA) and 0.25% Triton-X (Merck, Darmstadt, Germany). Subsequently, sections were incubated for 48 h at 4°C in the same solution with mouse anti-NeuN (1:2000; Chemicon; MAB377, Temecula, CA, USA). Sections were then processed with a secondary biotinylated horse antimouse IgG antibody (1:200, Vector Laboratories, Burlingame, CA, USA). They were then incubated for 1 h in an avidin-biotin-peroxidase complex (Vectastain ABC Elite PK6100, Vector) and, finally, with the chromogen 3,3′-diaminobenzidine tetrahydrochloride (DAB; Sigma-Aldrich, St. Louis, MO, USA). Sections were then dehydrated, cleared with xylene and cover-slipped.

Electron Microscopy

EC sections were postfixed for 24 h in a solution containing 2% paraformaldehyde, 2.5% glutaraldehyde (TAAB, G002, UK) and 0.003% $CaCl_2$ (Sigma, C-2661-500G, Germany) in sodium cacodylate (Sigma, C0250-500G, Germany) buffer (0.1 M). These sections were washed in sodium cacodylate buffer (0.1 M) and treated with 1% OsO_4 (Sigma, O5500, Germany), 0.1% potassium ferrocyanide (Probus, 23 345, Spain) and 0.003% $CaCl_2$ in sodium cacodylate buffer (0.1 M) for 1 h at room temperature. After washing in PB, sections were stained with 2% uranyl acetate (EMS, 8473, USA), and then dehydrated and flat-embedded in Araldite (TAAB, E021, UK) for 48 h at 60°C (DeFelipe and Fairén 1993). Embedded sections were glued onto a blank Araldite block and trimmed. Semithin sections (1–2 µm thick) were obtained from the surface of the block and stained with 1% toluidine blue (Merck, 115 930, Germany) in 1% sodium borate (Panreac, 141 644, Spain). The last semithin section (which corresponds to the section immediately adjacent to the block surface) was examined under light microscope and photographed to accurately locate the neuropil regions to be examined (Fig. 2).

Three-Dimensional Electron Microscopy

The 3D study of the samples was carried out using a dual-beam microscope (Crossbeam® 540 electron microscope, Carl Zeiss NTS GmbH, Oberkochen, Germany). This instrument combines

Table 1 Clinical and neuropsychological information

Case	Sex	Age (years)	Cause of death	Postmortem delay (h)	Neuropsychological diagnosis
AB1	Male	45	Lung cancer	<1	No neurological alterations
AB3	Male	53	Bladder carcinoma	3.5	No neurological alterations
IF10	Male	66	Bronchopneumonia and cardiac failure	2	No neurological alterations
M16	Male	40	Traffic accident	3	No neurological alterations

Note: None of the four subjects had recorded neurological or psychiatric alterations.

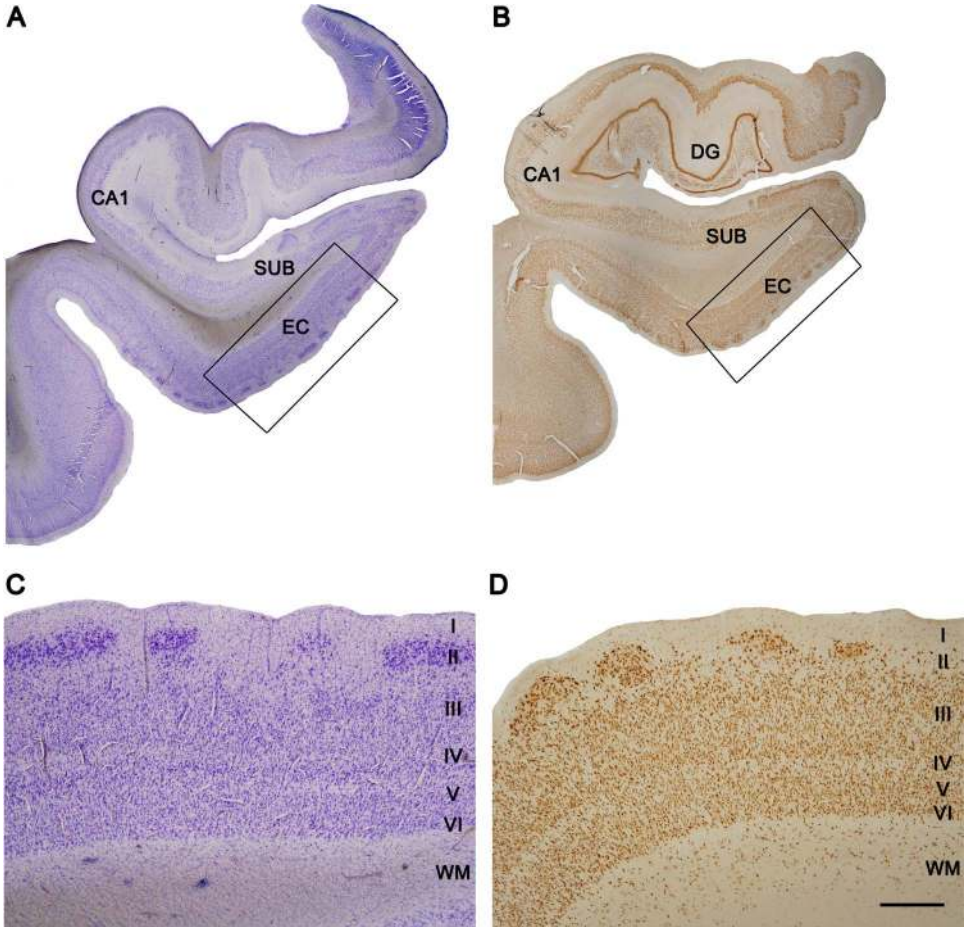

Figure 1. Coronal sections of the human hippocampal formation. (*A*, *B*) Low-power photographs showing the human EC (boxed areas). (*C*, *D*) Higher magnification of the boxed areas in *A* and *B*, to show the laminar pattern of EC (layers I to VI are indicated). Sections are stained for Nissl (*A*, *C*) and immunostained for anti-NeuN (*B*, *D*). WM, white matter. Scale bar (in *D*): 3 mm in panels *A* and *B*; 600 µm in panels *C* and *D*.

a high-resolution field-emission SEM column with a focused gallium ion beam (FIB), which the permits removal of thin layers of material from the sample surface on a nanometer scale. As soon as one layer of material (20 nm thick) is removed by the FIB, the exposed surface of the sample is imaged by the SEM using the backscattered electron detector. The sequential automated use of FIB milling and SEM imaging allowed us to obtain long series of photographs of a 3D sample of selected regions (Merchán-Pérez et al. 2009). Image resolution in the xy plane was 5 nm/pixel. Resolution in the z-axis (section thickness) was 20 nm, and image size was 2048 × 1536 pixels. Although the resolution of FIB/SEM images can be increased, we chose these parameters as a compromise solution to obtain a large enough field of view where synaptic junctions could still be clearly identified (Fig. 2) in a reasonable time period that allowed us to have long series of sections (approximately 12 h per stack of images).

The number of sections per stack from layer II ranged from 244 to 320, which corresponds to a raw volume ranging from 384 to 503 µm^3 (mean: 454 µm^3). A total of 12 stacks of images of the layer II neuropil were obtained (three stacks for each of the four cases; total volume studied: 5445 µm^3). For layer III, the number of sections per stack ranged from 268 to 313, corresponding to a corrected volume ranging from 423 to 492 µm^3 (mean: 456 µm^3). A total of 12 stacks of layer III neuropil images were obtained (three stacks for each of the four cases; total volume studied: 5466 µm^3).

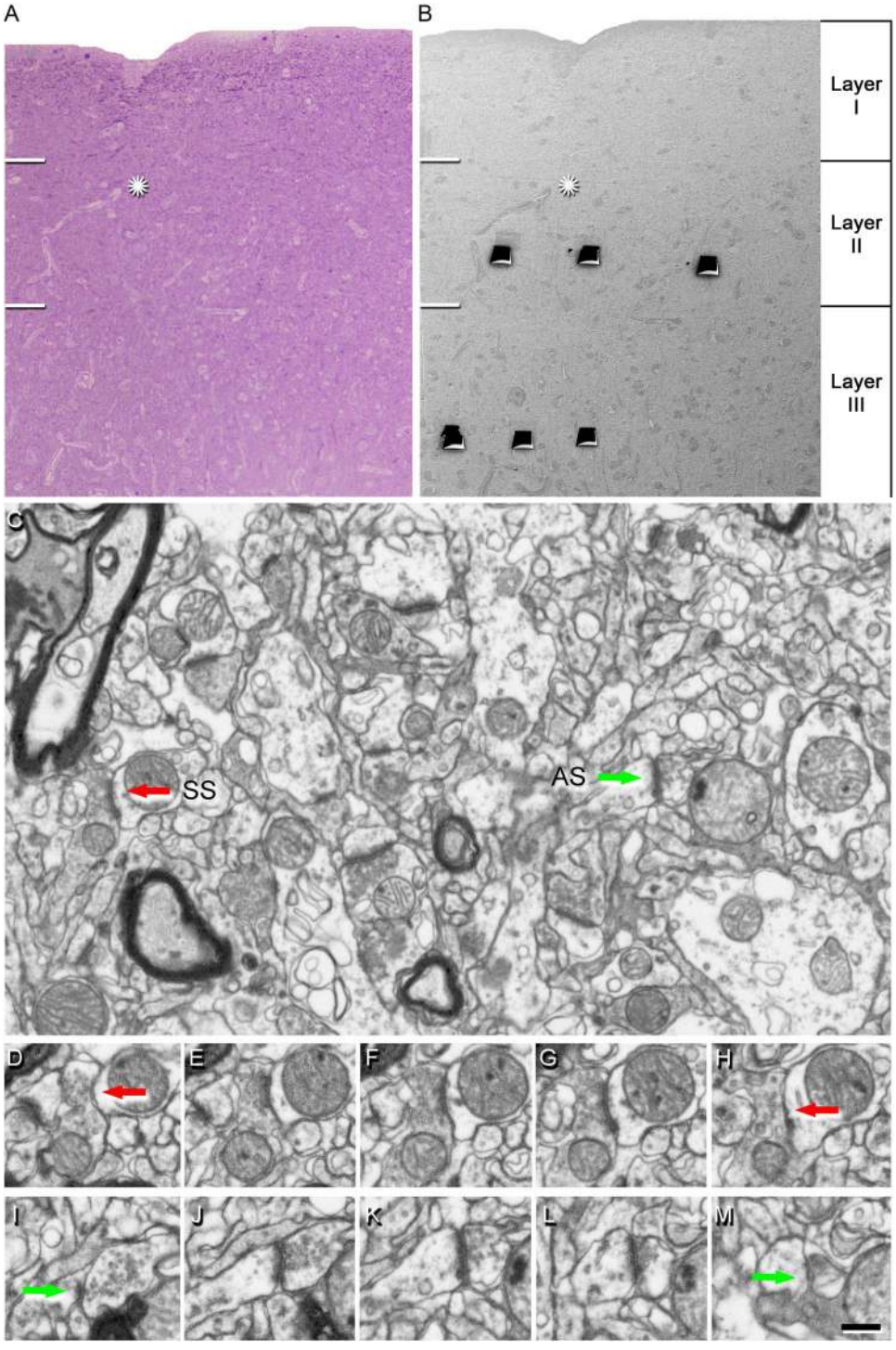

Figure 2. Correlative light/electron microscopy analysis of layer II and III of the EC. The delimitation of layers is based on the staining pattern of 1 µm-thick semithin section, stained with toluidine blue (*A*), which is adjacent to the block for FIB/SEM imaging (*B*). (*B*) SEM image to illustrate the block surface with trenches made in the neuropil (three per layer). Asterisks in *A* and *B* point to the same blood vessel, showing that the exact location of the region of interest was accurately determined. (*C*) Serial image obtained by FIB/SEM from layer II showing the neuropil, with two synapses indicated as examples of AS (green arrow) and SS (red arrow). Synapse classification was based on the examination of the full sequence of serial images; an SS can be visualized in *D*–*H*, and an AS in *I*–*M*. Scale bar (in *M*): 40 µm in *A*; 60 µm in *B*; 1000 nm in *C*; 1300 nm in *D*–*M*.

Table 2 Accumulated data obtained from the ultrastructural analysis of neuropil from layer II and layer III of the EC

EC layer	No. AS	No. SS	No. all synapses	% AS (mean ± SD)	% SS (mean ± SD)	CF volume (μm^3)	No. AS/μm^3 (mean ± SD)	No. SS/μm^3 (mean ± SD)	No. synapses/ μm^3 (mean ± SD)
II	1553	137	1690	91.90 ± 2.62	8.10 ± 2.62	4221	0.37 ± 0.05	0.03 ± 0.01	0.40 ± 0.03
III	1747	130	1877	92.84 ± 1.97	7.16 ± 1.978	4371	0.40 ± 0.09	0.03 ± 0.01	0.43 ± 0.01

Note: All volume data are corrected for fixation artifacts and shrinkage factor. Table sums up data from the four cases analyzed. The data for individual cases are shown in Supplementary Table 1.
SD, standard deviation.

A correction in the volume of the stack of images to account for the presence of fixation artifact (i.e., swollen neuronal or glial processes) was applied after quantification with Cavalieri principle (Gundersen et al. 1988). Every FIB/SEM stack was examined and the volume artifact ranged from 3 to 16% of the volume stacks.

All measurements were corrected for tissue shrinkage that occurs during osmication and plastic embedding of the vibratome sections containing the area of interest (Merchán-Pérez et al. 2009). To estimate the shrinkage in our samples, we photographed and measured the vibratome sections with ImageJ (ImageJ 1.51; NIH, USA), both before and after processing for EM. The values after processing were divided by the values before processing to obtain the volume, area, and linear shrinkage factors (Oorschot et al. 1991), yielding correction factors of 0.90, 0.93, and 0.97, respectively. A total of 24 stacks of images from both layers of the EC were obtained (three stacks per case and layer for each of the four cases, with a total corrected volume studied of 8592 μm^3 Table 2).

Synaptic Three-Dimensional Analysis

Stacks of images obtained by FIB/SEM were analyzed using EspINA software (*EspINA Interactive Neuron Analyzer*, 2.1.9; https://cajalbbp.es/espina/), which allows the segmentation of synapses in the reconstructed 3D volume (for a detailed description of the segmentation algorithm, see Morales et al. 2011; Fig. 3). As previously discussed in (Merchán-Pérez et al. 2009), there is a consensus for classifying cortical synapses into AS synapses (or type I) and SS (or type II). The main characteristic distinguishing these synapses is the prominent or thin postsynaptic density, respectively. Nevertheless, in single sections, the synaptic cleft and the pre- and postsynaptic densities are often blurred if the plane of the section does not pass at right angles to the synaptic junction. Since EspINA allows navigation through the stack of images, it was possible to unambiguously identify every synapse as AS or SS, based on the thickness of the post-synaptic density (PSD) (Merchán-Pérez et al. 2009). Synapses with prominent PSDs are classified as AS, whereas thin PSDs are classified as SS (Gray 1959; Peters and Palay 1996; Fig. 2). EspINA provided the number of synapses in a given volume, which allowed the estimation of the number of synapses per volume. EspINA also allowed the application of an unbiased 3D counting frame (CF) to perform direct counting (for details, see Merchán-Pérez et al. 2009).

In addition, geometrical features—such as size and shape—and spatial distribution features (centroids) of each reconstructed synapse were also calculated by EspINA. This software also extracts the Synaptic Apposition Surface (SAS) and provides its morphological measurements (Fig. 3). Since the pre- and postsynaptic densities are located face to face, their surface areas are comparable (for details, see Morales et al. 2013). Since the SAS comprises both the active zone and the PSD, it is a functionally relevant measure of the size of a synapse (Morales et al. 2013).

To identify the postsynaptic targets of the synapses, we navigated the image stack using EspINA to determine whether the postsynaptic element was a dendritic spine (spine or spines, for simplicity) or a dendritic shaft. Unambiguous identification of spines requires the spine to be visually traced to the parent dendrite. Similarly, for dendritic shafts to be unambiguously identified, they must be visually followed inside the stack. Accordingly, when the postsynaptic element of a synapse was close to the margins and was truncated by the borders of the stack, the identity of the postsynaptic target could not be determined. Therefore, the targets of synapses in each of the stacks were classified into two main categories: spines and dendritic shafts, whereas truncated elements that could not be safely identified were discarded. When the postsynaptic target was a spine, we further recorded the position of the synapse on the head or neck. Dendritic shafts were further classified as spiny (when dendritic spines could be observed emerging from the shaft) or aspiny. We also recorded the presence of single or multiple synapses on a single spine.

Spatial Distribution Analysis of Synapses

To analyze the spatial distribution of synapses, spatial point-pattern analysis was performed as described elsewhere (Anton–Sanchez et al. 2014; Merchán-Pérez et al. 2014). Briefly, we compared the actual position of centroids of synapses with the complete spatial randomness (CSR) model—a random spatial distribution model that defines a situation where a point is equally likely to occur at any location within a given volume. For each of the 24 different samples, we calculated three functions commonly used for spatial point-pattern analysis: F, G and K functions (for a detailed description, see Blazquez-Llorca et al. 2015). This study was carried out using the spatstat package and R Project program (Baddeley et al. 2015).

Statistical Analysis

To determine possible differences between layers, statistical comparisons of synaptic density, as well as size of the SAS, were carried out using the unpaired Mann–Whitney (MW) nonparametric U-test (when the normality and homoscedasticity criteria were not met) or *t*-test parametric test (when the normality and homoscedasticity criteria were met). To identify possible differences within a layer regarding the synaptic size (SAS) related to the shape of the synapses and their postsynaptic target, a Kruskal–Wallis nonparametric test (when the normality and homoscedasticity criteria were not met) or analysis of

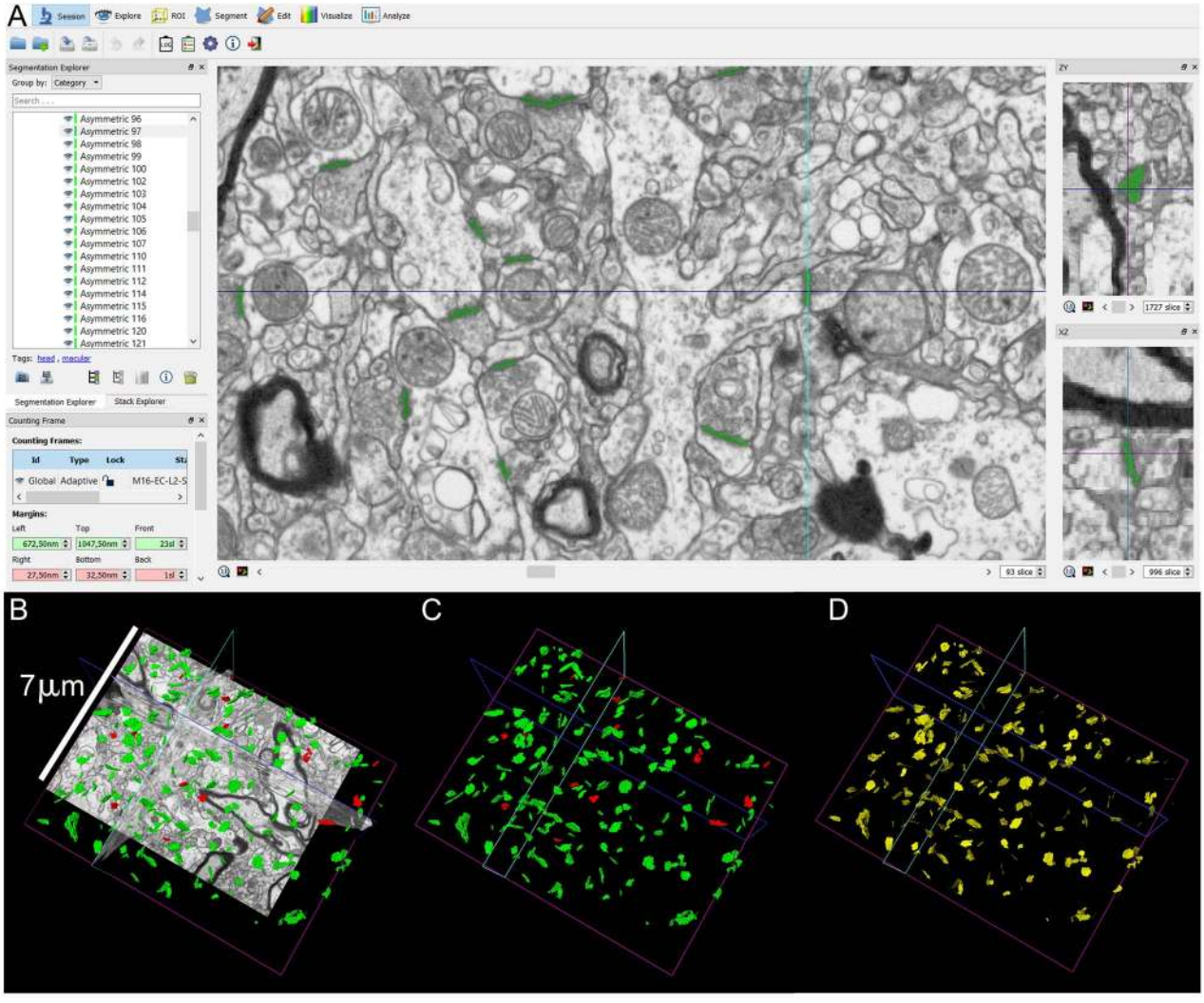

Figure 3. Screenshot of the EspINA software user interface. (*A*) In the main window, the sections are viewed through the xy plane (as obtained by FIB/SEM microscopy). The other two orthogonal planes, yz and xz, are also shown in adjacent windows (on the right). The 3D windows (*B*–*D*) show the three orthogonal planes and the 3D reconstruction of AS (green) and SS (red) segmented synapses (*B*), the reconstructed synapses (*C*), and the computed SAS for each reconstructed synapse (in yellow; *D*). Scale bar (in *B*): 7 µm in *B*–*D*.

variance (ANOVA) test were performed (when the normality and homoscedasticity criteria were met). Frequency distribution analysis of the SAS was performed using Kolmogorov–Smirnov (KS) nonparametric test. To perform statistical comparisons of AS and SS proportions regarding their synaptic morphology and their postsynaptic target, chi-square (χ^2) test was used for contingency tables. The same method was used to study whether there were significant differences between layers in relation to the shape of the synaptic junctions and their postsynaptic target.

Statistical studies were performed using the GraphPad Prism statistical package (Prism 7.00 for Windows, GraphPad Software Inc., USA).

Results

Coronal sections of the human EC at medial level were used for the present study (reviewed in Insausti et al. 2017). The EC was delimited by combining the Nissl and anti-NeuN markers (Fig. 1). The main cytoarchitectural characteristic of layer II (also called Pre-α) is the presence of large islands of modified pyramidal neurons and stellate cells (Braak and Braak 1992; Insausti and Amaral 2012; Kobro-Flatmoen and Witter 2019).

Synaptic Density

All the synapses reported, counted and analyzed in the present study were individually identified and segmented. The synaptic density values were obtained by dividing the total number of synapses included within the stereological CF by the total volume of the CF.

In the layer II samples, a total of 2310 synapses were identified and reconstructed in 3D, of which 1690 synapses were analyzed, after discarding incomplete synapses or those that were touching the exclusion edges of the stereological CF in a total volume of 4221 µm^3. Similarly, in the layer III samples, a total of 2580 synapses were identified and reconstructed in 3D, of which 1877 synapses were analyzed in a total volume of 4371 µm^3.

Table 3 Area (nm^2) and perimeter (nm) of the SAS from layer II and layer III of the EC

EC layer	Type of synapse (no. of synapses)	Area of SAS (nm^2)	Perimeter of SAS (nm)
II	AS (1553)	110 311 ± 3229	1631 ± 47
	SS (137)	65 997 ± 6041	1404 ± 73
III	AS (1747)	124 183 ± 3265	1826 ± 67
	SS (130)	67 445 ± 3243	1399 ± 75

Note: Data of the absolute number of synapses studied per layer and type are in parentheses. All data are corrected for shrinkage factor and are expressed as mean ± standard error of the mean. The data for individual cases are shown in Supplementary Table 2.

The average synaptic density of the EC layer II was 0.40 synapses/μm^3 (with a range of 0.38–0.43 synapses/μm^3; Table 2; Supplementary Fig. S1; Supplementary Table S1). In layer III, synaptic density was 0.43 synapses/μm^3 (with a range of 0.41–0.44 synapses/μm^3; Table 2; Supplementary Fig. S1; Supplementary Table S1). No differences in synaptic density between layers were observed (MW, $P = 0.18$).

Proportion of Excitatory and Inhibitory Synapses

Since each synapse was fully reconstructed in 3D, it was possible to precisely distinguish between AS and SS (Figs 2 and 3).

In layer II of the EC, the proportion of AS:SS was 92:8, and in layer III this ratio was 93:7 (Table 2; Supplementary Table S1). To statistically evaluate whether this difference in the ratio between the two layers was significant, chi-square (χ^2) tests were applied to 2 × 2 contingency tables, considering the two layers versus the two types of synapses, and no significant differences were found between layers (χ^2, $P = 0.18$).

Three-Dimensional Spatial Synaptic Distribution

To analyze the spatial distribution of the synapses, the actual position of each of the synapses in each stack of images was compared with a random spatial distribution model CSR. For this, the functions F, G and K were calculated. In the image stacks analyzed (12 from EC layer II and 12 from EC layer III), the three spatial statistics functions resembled the theoretical curve that simulates the random spatial distribution pattern, which indicated that synapses fitted a random spatial distribution model (Supplementary Fig. S2).

Study of the Characteristics of the Synapses

Synaptic Size

The study of the synaptic size was carried out analyzing the characteristics of the area and the perimeter of the SAS of each synapse identified and 3D reconstructed in all samples (Fig. 3).

In layer II, the average area of the SAS for the AS was 110 311 nm^2 and 65 997 nm^2 in the case of SS (Table 3; Supplementary Table S2). When the average sizes of the two types of synapses were compared, it was found that the area of the AS was significantly larger than the area of the SS (MW, $P = 0.03$). This difference was also found in the frequency distribution of the area (KS, $P < 0.0001$), indicating that the AS were larger than the SS.

In layer III, the average area of the SAS for AS was 124 183 nm^2 and 67 445 nm^2 in the case of SS (Table 3; Supplementary Table S2). When comparing the two types of synapses, it was found that both the area and the perimeter of the AS were significantly larger than the same parameters in the SS (MW, $P = 0.03$). These differences were also found in the frequency distributions of the area and perimeter (KS, $P < 0.0001$), indicating that the AS were larger than the SS, as occurred in layer II.

Statistical comparisons between layers showed differences in the average size of the AS area (MW, $P = 0.03$; Fig. 4A). This statistical difference between layers was also found in the frequency distribution of the area and perimeter of AS (KS, $P < 0.0001$; Fig. 4B, C). In summary, AS in layer III were larger than in layer II, whereas no differences were found for SS.

Synaptic Shape

Regarding shape, the synapses were classified into four categories: macular (with a flat, disk-shaped PSD), perforated (with one or more holes in the PSD), horseshoe (with an indentation in the perimeter of the PSD) or fragmented (with two or more physically discontinuous PSDs; Supplementary Fig. S3A; for a detailed description, see Santuy et al. 2018a; Domínguez-Álvaro et al. 2019).

In layer II, a total of 1549 AS were identified and reconstructed in 3D, with 83% presenting a macular morphology, followed by 12.9% perforated, 3.3% horseshoe, and 0.8% fragmented (Fig. 5A). As for the SS, a total of 137 synapses were identified and reconstructed in 3D, with the majority presenting a macular morphology (73%). Of the remaining SS, 15.3% were horseshoe-shaped, 11% were perforated, and 0.7% were fragmented (Table 4; Supplementary Table S3). Determining the proportions of the two categories (i.e., AS and SS; Fig. 5B) for each synapse shape revealed that, of the total macular synapses, 92.8% were AS and 7.2% were SS. This proportion was maintained in the case of perforated synapses (93% versus 7% SS), while it changed significantly in the case of the horseshoe synapses, where 70.8% were AS and 29.2% were SS (χ^2, $p < 0.0001$). Thus, SS showing a horseshoe shape were more frequent than expected according to the general proportion of SS (7%). In the case of fragmented synapses, the proportion was maintained (92.9% AS and 7.1% SS).

In the layer III samples, a total of 1746 AS were identified and reconstructed in 3D. Of these, the majority presented a macular morphology (75.9%), followed by perforated (19.9%) and horseshoe (3.3%), and only a small percentage of the AS presented a fragmented morphology (0.9%) (Fig. 5C). A significantly lower number of macular AS and a significantly higher number of perforated AS were found compared with layer II (χ^2, $P < 0.0001$). Of a total of 129 SS, 65.9% had a macular morphology, 15.5% had a perforated shape, 17% were horseshoe-shaped, and 1.6% had a fragmented morphology (Table 4; Supplementary Table S3). Regarding the prevalence of each type (AS and SS (Fig. 5D)), 94% of the macular morphology synapses were AS, whereas 6% were SS. This proportion was maintained in the perforated synapses (94.5% AS versus 5.5% SS); however,

Table 4 Proportion of the different shapes of synaptic junctions in layer II and layer III of the EC

EC layer	Type of synapse	Macular synapses	Perforated synapses	Horseshoe-shaped synapses	Fragmented synapses	Total synapses
II	AS	83.0% (1285)	12.9% (200)	3.3% (51)	0.8% (13)	100% (1549)
	SS	73.0% (100)	11.0% (15)	15.3% (21)	0.7% (1)	100% (137)
III	AS	75.9% (1326)	19.9% (347)	3.3% (58)	0.9% (15)	100% (1746)
	SS	65.9% (85)	15.5% (20)	17.0% (22)	1.6% (2)	100% (129)

Note: Data are given as percentages with the absolute number of synapses studied in parentheses. Data for each individual case are shown in Supplementary Table 3.

similar to the observations in layer II, this changed significantly in the case of horseshoe-shaped synapses, where 72.5% were AS and 27.5% were SS (χ^2, $p < 0.0001$). Thus, SS showing a horseshoe shape were more frequent than expected according to the general proportion of SS. In the case of the fragmented synapses, 88.2% corresponded to AS, whereas 11.8% were SS.

Synaptic Size and Shape

We also determined whether the shape of the synapses was related to their size. For this purpose, the area and perimeter of the SAS, of both AS and SS, were analyzed according to synaptic shape.

We found that, in both layer II and III samples, the area and perimeter of the macular AS were significantly smaller than the area and the perimeter of the perforated, horseshoe or fragmented AS (ANOVA, $P < 0.001$; Supplementary Fig. S3B–E). This tendency was also observed in SS (but no significant differences were found).

No differences were found in the synaptic size (measured as the average of the AS area and perimeter) between the two layers (MW, $P > 0.05$). No differences were found in the frequency distribution of the area and perimeter of AS (KS, $P > 0.01$).

Study of the Postsynaptic Elements

Postsynaptic targets were unambiguously identified and classified as spines and dendritic shafts. Additionally, when the postsynaptic element was a spine, we distinguished the location of the synapse on the neck or on the head of this spine. When the postsynaptic element was identified as a dendritic shaft, it was classified as "with spines" or "without spines" (for details, see Domínguez-Álvaro et al. 2019).

The postsynaptic elements of 1157 AS and 124 SS were determined in the layer II samples—50.3% of the AS were established on dendritic shafts (25.8% on dendritic shafts with spines and 24.5% on dendritic shafts without spines), 49.0% of the AS were established on spine heads and 0.7% on spine necks. In the case of SS, 88% were established on dendritic shafts (63% on dendritic shafts with spines and 25% on dendritic shafts without spines), whereas 10.4% were established on spine heads, and the remaining 1.6% were on spine necks (Table 5; Supplementary Table S4).

Considering all types of synapses established on the spine heads, the proportion of AS:SS was 98:2, whereas in those established on dendritic shafts, this proportion was 84:16. Since the overall AS:SS ratio in layer II was 92:8, the present results show that AS and SS did show a preference for a particular postsynaptic element, that is, the AS showed a preference for the spine heads, whereas the SS showed a preference for the dendritic shafts (χ^2, $P < 0.0001$; Fig. 6A).

Grouping by both type of synapse (AS or SS) and type of postsynaptic target (spine head, spine neck or dendritic shaft), it was found that 45.4% of layer II synapses were AS established on dendritic shafts, closely followed by AS on spine heads (44.3%), whereas 8.5% were SS on dendritic shafts, and 1.0% were SS on spine heads. The two least frequent types of synapses were AS and SS established on spine necks (0.6% and 0.2%, respectively; Fig. 6B).

Regarding the samples of layer III, the postsynaptic elements of 1367 AS and 120 SS were analyzed; 52.4% of the AS were located on dendritic shafts (20.6% on dendritic shafts without spines, 31.8% on dendritic shafts with spines), whereas 46.7% of AS were established on spine heads and 0.9% on necks. Most of the SS were established on dendritic shafts (61.7% on dendritic shafts with spines and 22.5% on dendritic shafts without spines), whereas 13.3% were found on spine heads and 2.5% on necks (Table 5; Supplementary Table S4).

When the preference of the synaptic types (AS or SS) for a particular postsynaptic element was analyzed, we found that the AS presented a statistically significant preference for spine heads (χ^2, $P < 0.0001$); whereas the SS showed a significant preference for dendritic shafts (χ^2, $P < 0.0001$; Fig. 6C), in line with what we found in layer II.

Analysis of synapses established on spine heads showed an AS:SS ratio of 98:2, whereas in dendritic shafts, the AS:SS ratio was 88:12. Given that the general ratio of AS and SS in layer III was 92:8, it could be concluded that the AS presented preference for the spine heads and the SS for the dendritic shafts (χ^2, $P < 0.0001$; Fig. 6C), similar to our observations in layer II. In the case of synapses on dendritic necks, although a higher proportion of SS was observed compared with what would be expected by chance, the SS sample was not large enough to draw statistically reliable conclusions.

Simultaneously considering synaptic types and postsynaptic targets, we found similar results to layer II: 48.1% were AS on dendritic shafts, followed by AS on spine heads (43.0%), whereas 6.8% were SS on dendritic shafts, and 1.1% were SS on spine heads. The less frequent types of synapses were AS and SS established on spine necks (0.8% and 0.2%, respectively; Fig. 6D).

Statistical comparisons of the proportion of AS (χ^2, $P = 0.30$) and SS (χ^2, $P = 0.46$) established on spines and dendritic shafts did not show differences between layers II and III.

Table 5 Distribution of AS and SS on spines and dendritic shafts in layer II and layer III of the EC

EC layer	Type of synapse	Synapses on spine heads	Synapses on spine necks	Synapses on aspiny dendritic shaft	Synapses on spiny dendritic shaft	Total synapses
II	AS	49.0% (567)	0.7% (8)	24.5% (284)	25.8% (298)	100% (1157)
	SS	10.4% (13)	1.6% (2)	25.0% (31)	63.0% (78)	100% (124)
III	AS	46.7% (639)	0.9% (12)	20.6% (281)	31.8% (435)	100% (1367)
	SS	13.3% (16)	2.5% (3)	22.5% (27)	61.7% (74)	100% (120)

Note: Synapses on spines have been sub-divided into those established on spine heads and those established on spine necks. Moreover, we differentiated between aspiny and spiny dendritic shafts. Data are given as percentages with the absolute number of synapses studied in parentheses. Data for each individual case are shown in Supplementary Table 4.

Finally, to detect the presence of multiple synapses, an analysis of the synapses established on spine heads was performed. In layer II, the most frequent finding was a single AS per head (90.3%), followed by two AS (5.5%), whereas 3.8% had one AS and one SS on a head, and the frequency of a single SS per head was very low (0.4%; Fig. 7). Likewise, in layer III, the most frequent finding was the presence of a single AS on a head (89.6%), followed by two AS (6.1%), whereas only 3.7% had one AS and one SS on the same head, and the least frequent combinations were a single SS and two SS on a head (0.3% and 0.3%, respectively; Fig. 7).

Postsynaptic Elements and Synaptic Size

In addition to the study of the distribution of synapses in the different postsynaptic elements, we analyzed whether there was a relationship between the synapse size and the type of postsynaptic element. The study was carried out with the data of the area and perimeter of the SAS of each synapse whose postsynaptic element was identified.

In layer II, AS established on spine necks were smaller than AS established on dendritic heads or shafts (ANOVA, $P < 0.0001$; Supplementary Fig. S4). However, in the samples from layer III, no statistically significant differences were found in the size of the AS established on spine heads, spine necks, or dendritic shafts (ANOVA, $P > 0.05$; Supplementary Fig. S4). In the case of SS, their numbers were too low to perform a robust statistical analysis.

The comparison between layers regarding the size of the synapses according to the postsynaptic element did not show any difference (MW, $p > 0.05$). However, we found differences between layers regarding the frequency distribution of the SAS perimeter of the AS established on dendritic shafts (KS, $p = 0.0005$)—larger synapses were more frequent on the dendritic shafts in layer III. This finding is in line with the results in layer III regarding the larger size of AS and the higher proportion of perforated AS synapses.

Discussion

The following major results were obtained: (1) synaptic density and ratio were quite similar in both layers, (2) synapses fitted into a random spatial distribution in both layers, (3) in both layers, AS were larger than SS, and in layer III, AS were larger than in layer II; (4) regardless of the layer, most synapses are AS and display a macular shape—and there is an almost equal split between the targeting of dendritic shafts and spines. As far as we know, detailed 3D synaptic morphology analysis and identification of postsynaptic targets at the ultrastructural level have not been performed before in the human EC.

Synaptic Density

Synaptic density is critical not only to describe the synaptology of a particular brain region, but also in terms of connectivity. The mean synaptic density in EC was 0.42 synapses/μm^3 and was similar in layer II (0.40 synapses/μm^3) and III (0.43 synapses/μm^3). These values are higher than those reported by Scheff et al. (1993) using transmission electron microscopy (TEM). These authors estimated a density of 0.32 synapses/μm^3 in layer III of EC. This difference may arise not only from differences in age of the human brain tissue used—4 individuals aged 40, 45, 53, and 65 years old in our study versus 11 individuals aged 60–83 years old in the study by Scheff et al. (1993)—, but also from the method used to estimate synaptic density. Perhaps more importantly, in the TEM study, synaptic density was calculated using estimations based on the number of synaptic profiles per unit area (size-frequency method) in single ultrathin sections of tissue. That is, the number of synapses per volume unit is estimated from two-dimensional samples. As previously discussed (Merchán-Pérez et al. 2009), FIB/SEM technology provides the *actual* number of synapses per volume unit, and it avoids most of the errors associated with stereological methods. In addition, our current data are very similar within cases, showing very little variability between samples (Supplementary Table S1; Supplementary Fig. S1), suggesting a robust estimation of the synaptic.

Our previous study using FIB/SEM in layer II of the human transentorhinal cortex (TEC) showed a mean synaptic density of 0.41, 0.42, and 0.43 synapses/μm^3 in cases AB1, IF10 and M16, respectively—three cases that were also analyzed in the present study (Domínguez-Álvaro et al. 2018). Moreover, estimations performed in human CA1 hippocampal region, also using FIB/SEM technology, have shown (in cases AB1 and AB3) a synaptic density in the stratum oriens ranging from 0.39 and 0.43 synapses/μm^3, respectively, and 1.09 synapses/μm^3 in the superficial part of the stratum pyramidale in both cases (Montero-Crespo et al. 2020). Since the processing and analysis methods were identical, these similarities (with layer II from TEC and stratum oriens of CA1) and differences (with

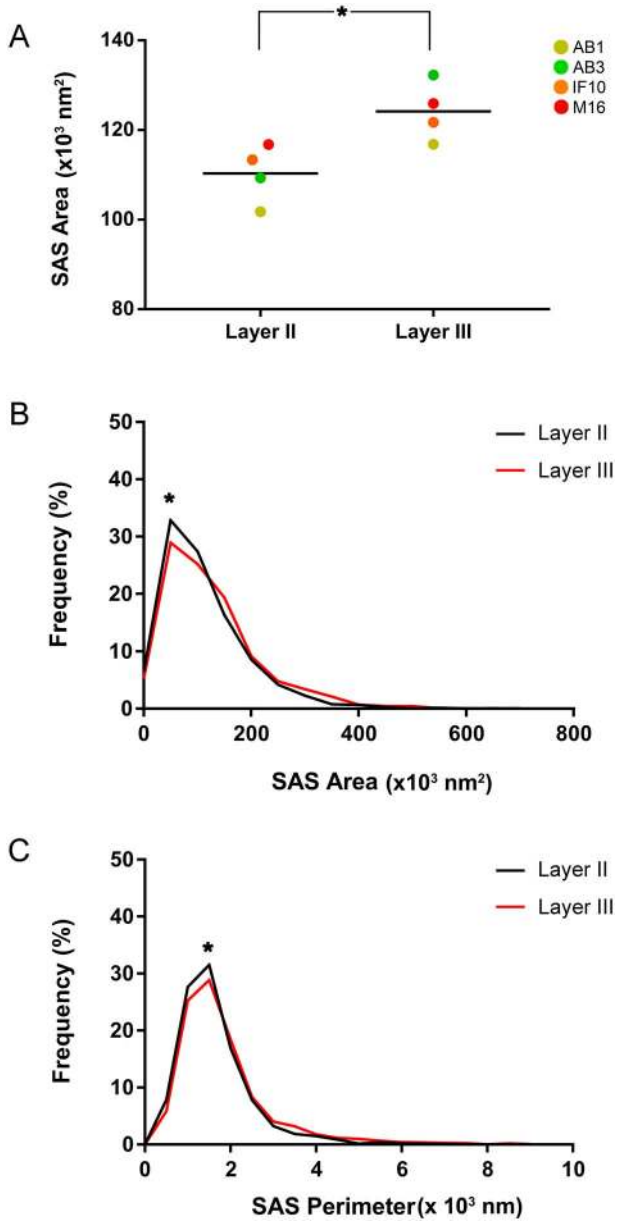

Figure 4. Graph showing the mean AS SAS area (*A*), and the frequency distribution plots of AS SAS area (*B*), and perimeter (*C*), in layers II and III of the EC. A different color corresponds to each analyzed case, as denoted in the key (*A*). Statistical comparisons between layers showed differences in the size of the AS area (*A*) (asterisk; MW, $P = 0.03$), as well as in the frequency distribution of the area (*B*) and perimeter (*C*) (KS, $P < 0.0001$; indicated with an asterisk).

CA1 pyramidal layer) may be attributable to the specific layer and brain region analyzed, suggesting that synaptic density greatly depends on the human brain layer and/or region being studied.

Proportion of Synapses and Spatial Synaptic Distribution

In the cerebral cortex, there are two major morphological types of synapses, type I and type II (Gray 1959), which correspond, respectively, to the AS and SS types described by Colonnier (1968) (see also, Peters 1987; Peters et al. 1991; Peters and Palay 1996). In general, AS are considered to be excitatory and SS inhibitory (Ribak 1978; for reviews, see Houser et al. 1984; White 1989; DeFelipe and Fariñas 1992; Freund and Buszsaki 1996; Somogyi et al. 1998). Therefore, at the circuit level, the proportion of excitatory and inhibitory synapses is critical from a functional point of view, since higher or lower proportions are linked to differences in the excitatory/inhibitory balance of the cortical circuits (for reviews, see Froemke 2015; Zhou and Yu 2018; Sohal and Rubenstein 2019).

Previous studies have shown that the percentage of AS and SS varied between 80–95% and 20–5%, respectively, in all the cortical layers, cortical areas and species examined so far by TEM (reviewed in DeFelipe 2015; Beaulieu and Colonnier 1985; Bourne and Harris 2011; DeFelipe et al. 2002; DeFelipe 2011; Megías et al. 2001). In the present study, the proportion of AS and SS was similar in layers II (92% and 8%, respectively) and III (93% and 7%) of the EC, and these values were also similar to previous results, also using FIB/SEM, in the human TEC (96% and 4%; Domínguez-Álvaro et al. 2018) and in the human CA1 hippocampal field (95% and 5%, except in the stratum lacunosum-moleculare, which was 89% and 11%; Montero-Crespo et al. 2020). Thus, it seems that in the human cerebral cortex the percentage of AS and SS are among the highest and lowest proportions, respectively, previously observed in the cerebral cortex in general using TEM. The significance of this relatively high and low proportion of AS and SS, respectively, and the invariance of this proportion in the human cerebral cortex, is difficult to interpret because of the differences in the cytoarchitecture, connectivity and functional characteristics of the different cortical regions. For example, layer II of the EC contains numerous spiny stellate-neurons, modified pyramidal neurons and a small proportion of bi- and multipolar neurons. However, in layer III, the most abundant neuronal type is the pyramidal neuron, although bi- and multipolar neurons are also present (reviewed in Kobro-Flatmoen and Witter 2019). In addition, a variety of morphological, neurochemical and functional types of GABAergic interneurons are present in both layers but their distribution and density seem to be different depending on the layer of the EC (Wouterlood et al. 1995; reviewed in Witter et al. 2017). For example, parvalbumin-positive interneurons are particularly abundant in layer II, whereas somatostatine-positive cells are more frequent in layer III (Wouterlood and Pothuizen 2000).

Furthermore, layer II receives excitatory inputs from cortical association areas, olfactory regions, presubiculum and parasubiculum and from neurons located in deep layers of the EC. Layer III receives excitatory inputs from these same regions, but also receives inputs from the claustrum and the amygdala (reviewed in Insausti and Amaral 2012). Finally, neurons in layers II and III receive inhibitory synaptic inputs originating from GABAergic neurons in the hippocampus (Ino et al. 1990; Melzer et al. 2012) and from a variety of local interneurons, whose functional roles and laminar specificity remain unclear (Kumar and Buckmaster 2006). Since the present results did not reveal differences in the AS:SS ratio between layer II and III in the neuropil, it could be interpreted that the proportion of AS and SS on the dendritic arbor of the different types of neurons may be similar. However, in other cortical regions of a variety of species, it has been shown that there are differences in the number of inputs of GABAergic and glutamatergic synapses in different neuronal types (e.g., DeFelipe and Fariñas, 1992; Freund and Buzsáki 1996; DeFelipe 1997; Somogyi et al. 1998; Schubert et al. 2007; Markram et al. 2015; Tremblay et al. 2016). Thus, it would

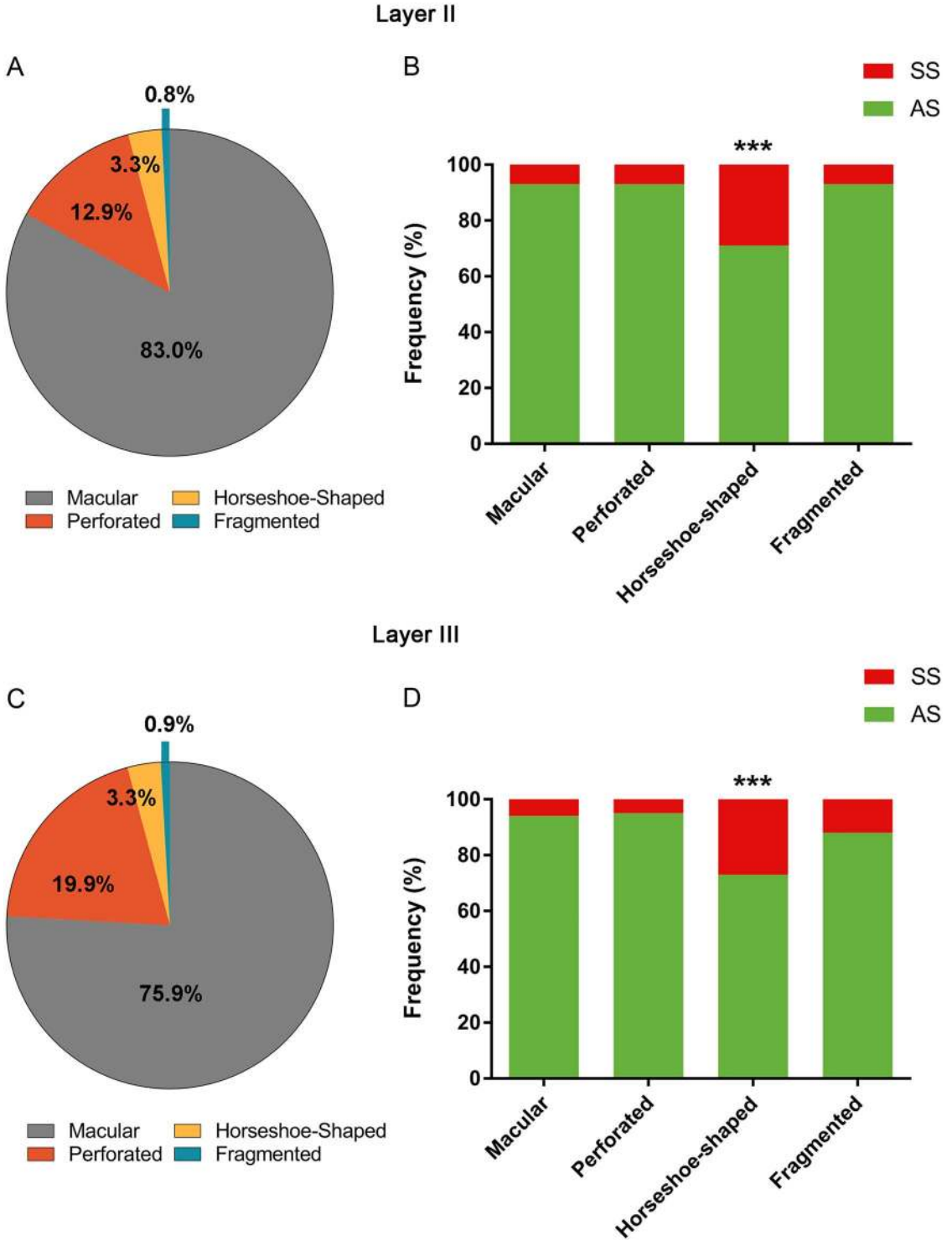

Figure 5. Proportions of the different synaptic shapes in layers II (*A*, *B*) and III (*C*, *D*) of the EC. (*A*) Shape proportions of the AS in layer II. (*B*) Proportions of AS and SS belonging to each shape type in layer II. (*C*) Shape proportions of the AS in layer III. A significantly fewer number of macular AS and a significantly higher number of perforated AS were found compared with layer II (asterisks; χ^2, $P < 0.0001$). (*D*) Proportions of AS and SS belonging to each shape type in layer III. In both layer II and layer III, the horseshoe-shaped synapses were significantly more frequent among SS than AS (asterisks; χ^2, $P < 0.0001$).

be necessary to examine the synaptic inputs on each particular cell type in the EC to determine possible differences in the AS:SS ratio in particular cell types, although the final general AS:SS ratio does not vary in the neuropil.

Finally, we would like to point out that although we only examined the neuropil, the study of the perisomatic innervation is also critical to better understand the synaptic organization of cortical circuits. Indeed, GABAergic inputs on the dendrites

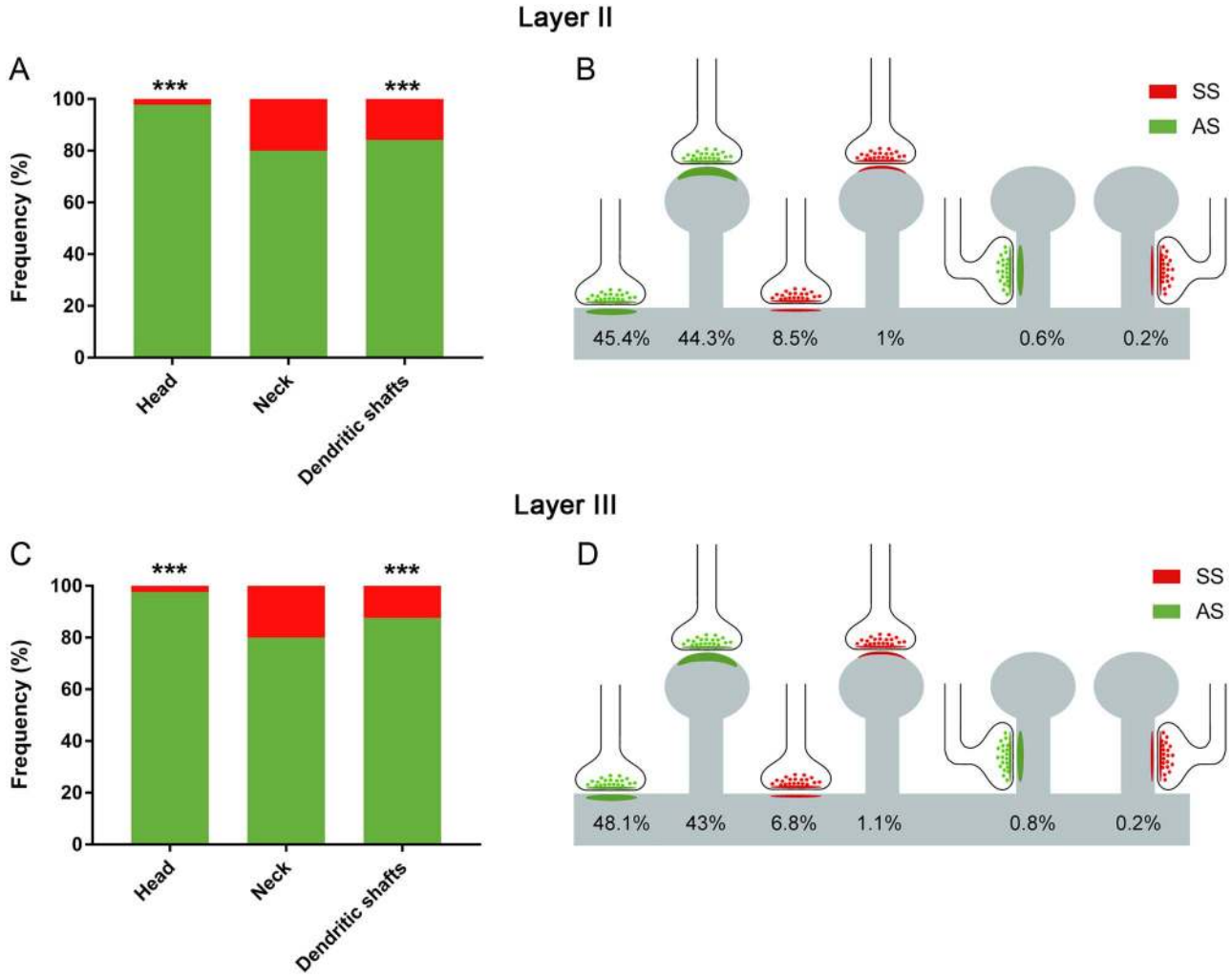

Figure 6. Analysis of the postsynaptic target distribution in layers II (*A*, *B*) and III (*C*, *D*) of the EC. (*A*) Graph showing the proportions of AS and SS corresponding to each postsynaptic target in layer II. (*B*) Schematic representation of the distribution of AS and SS on different postsynaptic targets in layers II. (*C*) Proportions of AS and SS corresponding to each postsynaptic target in layer III. In both layer II and layer III, the AS showed a preference for spine heads, whereas the SS showed a preference for dendritic shafts (asterisks; χ^2, $P < 0.0001$). (*D*) Schematic representation of the distribution of AS and SS on different postsynaptic targets in layer III. (*B*, *D*) Percentages of postsynaptic targets are indicated, showing —from left to right— the most frequent type (AS on dendritic shafts) to the least frequent type (SS on spine necks). (*A*–*D*) Synapses on spines have been sub-classified into those that are established on the spine head and those established on the neck.

and the somata of pyramidal cells originate from numerous and various morphological and functional axo-dendritic and basket cell types, whereas the main source of synapses on the axon initial segment is one or few chandelier cells (DeFelipe 2002; Freund and Buzsáki 1996). As discussed by Freund and Katona (2007), there seems to be clear functional dichotomy in the innervation of pyramidal cells. Interneurons that innervate the dendritic arbor of pyramidal cells are involved in the control of the efficacy and plasticity of glutamatergic inputs from specific sources that terminate in the same dendritic regions. By contrast, those interneurons innervating the perisomatic region control the output and the synchrony of action potentials of large populations of pyramidal cells. Therefore, further studies should be performed to examine the perisomatic innervation of particular types of neurons in the EC.

Regarding the spatial organization of synapses, we found that synapses were randomly distributed in the neuropil of both layers. This type of spatial distribution has also been found in the frontal and transentorhinal cortices, as well as in the CA1 hippocampal region of the human brain (Blazquez-Llorca et al. 2013; Domínguez-Álvaro et al. 2018; Montero-Crespo et al. 2020).

Therefore, the present results suggest that the random spatial distribution of synapses and the AS:SS ratio (ranging from 92 to 96% for AS and 8 to 4% for SS) are widespread "rules" of the synaptic organization of the human cerebral cortex.

Shape and Size of the Synapses

There are very few studies on human brain that provide data regarding the size of the synaptic junctions for comparison with our current results. Similar studies have been performed in layer IV of the temporal neocortex (Yakoubi et al. 2019a). Yakoubi's group analyzed 150 boutons establishing AS synapses and reported that the mean size of the active zone was 130 000 nm^2. These results are in line with our current measurements for the area of the SAS of AS in both layer II (110 311 nm^2) and

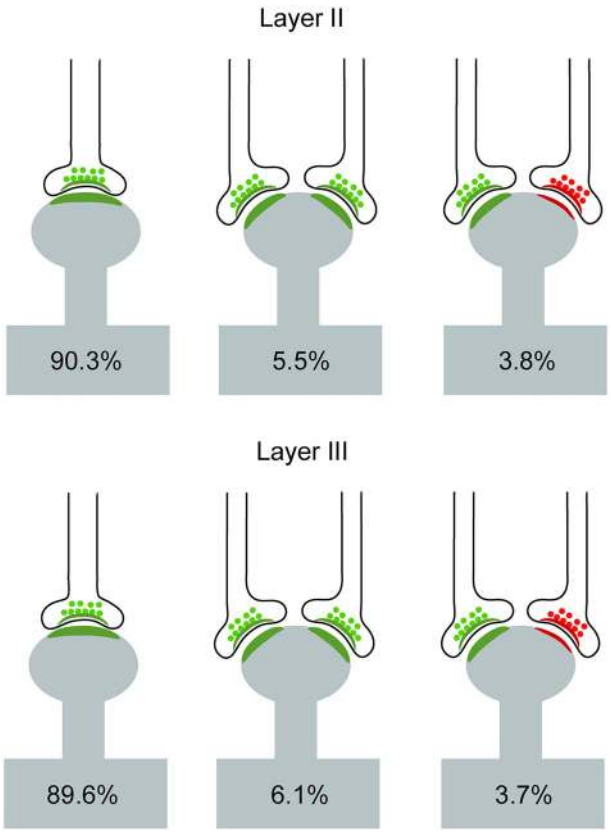

Figure 7. Schematic representation of single and multiple synapses on dendritic spine heads in layers II and III of the EC. Percentages of each type are indicated. Synapses on the necks and other combinations that were rarely found (less than 1%) have not been included. AS have been represented in green and SS in red.

layer III (124 183 nm^2), and also similar to our previous results in the human TEC (118 037 nm^2; Domínguez-Álvaro et al. 2018). In our studies on human EC and TEC, 3300 and 2545 axon terminals forming AS were analyzed, respectively, and they therefore represent robust data.

We also found that, in both EC layers, excitatory contacts (AS) were larger than inhibitory (SS) ones (117 247 vs. 66 721 nm^2, respectively), as was also observed in layer II of the human TEC (118 037 vs. 73 590 nm^2; Domínguez-Álvaro et al. 2019). Furthermore, we found that AS of layer III were significantly larger (124 183 nm^2) than those in layer II (110 311 nm^2), suggesting layer specific characteristics regarding synaptic size. Synaptic size has been proposed to correlate with release probability, synaptic strength, efficacy, and plasticity (Nusser et al. 1998; Takumi et al. 1999; Ganeshina et al. 2004a; Tarusawa et al. 2009; Holderith et al. 2012; Südhof 2012; Biederer et al. 2017).

Most EC synapses presented a macular shape (taking both layers together, 78% were macular), whereas 21% were the more complex-shaped synapses (perforated, horseshoe and fragmented)—both figures that are comparable with previous reports in different brain areas and species (Geinisman et al. 1987; Jones and Calverley 1991; Neuman et al. 2015; Santuy et al. 2018b; Domínguez-Álvaro et al. 2019; Montero-Crespo et al. 2020). Complex-shaped synapses are larger than macular ones. In particular, perforated synapses have more AMPA and NMDA receptors than macular synapses and are thought to constitute a relatively "powerful" population of synapses with more long-lasting memory-related functionality than macular synapses (Ganeshina et al. 2004a, 2004b; Spruston 2008; Vicent-Lamarre et al. 2018). Our current results also showed that macular AS were smaller than the complex-shaped synapses. In addition, macular synapses were less abundant in layer III than in layer II. Considering all types of synapses, AS in layer III were larger than those in layer II.

As mentioned above, neurons in layer III of the EC project to CA1 and the SUB, whereas those in layer II send their axons to DG and CA3. Moreover, upper EC layers receive afferents from a number of cortical regions as well as from the parahippocampal and perirhinal cortex (Schultz et al. 2015). Therefore, the differences in synaptic size observed between layer II and III may reveal unique microanatomical synaptic features that may be related to the differential pattern of layer connectivity in human EC.

Postsynaptic Targets

In the present work, the co-analysis of the synaptic type and postsynaptic target showed that the proportion of AS established on dendritic spines (also known as "axospinous") reached around 45–48% in both layer II and layer III of the EC. Using the same FIB/SEM technology, in layer II of the human TEC, we found that 55% of AS were established on dendritic spines (Domínguez-Álvaro et al. 2019), whereas in the human hippocampal CA1 field, this percentage was 87.22% (ranging from 71.70% in the *stratum lacunosum-moleculare* to 94.34% in *superficial stratum pyramidale*; Montero-Crespo et al. 2020). Furthermore, serial EM studies performed in layer IV and V of the human temporal neocortex have reported that axospinous AS account for approximately 77% and 85% of the AS, respectively (Yakoubi et al., 2019a, 2019b), whereas our preliminary data from FIB/SEM studies in layer III of the human temporal cortex—based on the 3D reconstruction of 1456 synapses—showed that 68% of AS were axospinous (Cano-Astorga et al., unpublished results). Therefore, there are important differences and similarities in the proportion of AS on spines and dendritic shafts in different cortical regions and layers, which may represent another microanatomical specialization of the cortical regions examined.

Conclusion

The present work constitutes a detailed description of the synaptic organization of the human EC, which is a necessary step to better understand its functional organization in both health and disease. Although our data are very robust because it is based on the analysis of thousands of synapses, the data were obtained from four individuals. Therefore, caution must be exercised when interpreting the significance of the results. Performing further studies on brain tissue from more subjects of different ages—including both males and females—will be necessary to better understand both the variability and invariance of human synaptic organization.

Supplementary Material

Supplementary Material can be found at *Cerebral Cortex* online.

Funding

Spanish "Ministerio de Ciencia e Innovación" (grant PGC2018-094307-B-I00); the Cajal Blue Brain Project (the Spanish partner of the Blue Brain Project initiative from EPFL, [Switzerland]);

Centro de Investigación Biomédica en Red sobre Enfermedades Neurodegenerativas, Spain (CB06/05/0066); the Alzheimer's Association (ZEN-15-321663); the European Union's Horizon 2020 Framework Programme for Research and Innovation (grant agreement No. 945539) to Human Brain Project SGA3; the Spanish "Ministerio de Educación y Formación Profesional" (FPU14/02245 to M.M.-C.); UNED (Plan de Promoción de la Investigación, 2014-040-UNED-POST to L.B.-L.) We acknowledge support of the publication fee by the CSIC Open Access Publication Support Initiative through its Unit of Information Resources for Research (URICI)..

Availability of data and materials

Most data are available in the main text or the supplementary materials. Data sets used and analyzed during the current study are also available from the corresponding author on reasonable request and they are published on the EBRAINS Knowledge Graph; DOI: 10.25493/3GMJ-FEZ (https://kg.ebrains.eu/search/instances/Dataset/21541277-0595-4aae-bd40-924fe70c83e8).

Notes

We would like to thank Carmen Álvarez and Lorena Valdés for their technical assistance, and Nick Guthrie for his excellent text editing. *Conflict of Interest:* None declared.

References

Anton-Sanchez L, Bielza C, Merchán-Pérez A, Rodríguez JR, DeFelipe J, Larrañaga P. 2014. Three-dimensional distribution of cortical synapses: a replicated point pattern-based analysis. *Front Neuroanat*. 8:85.

Baddeley A, Rubak E, Turner R. 2015. *Spatial point patterns: methodology and applications with R*. Boca Raton (CA): Chapman and Hall/ CRC Press.

Beaulieu C, Colonnier M. 1985. A laminar analysis of the number of round-asymmetrical and flat-symmetrical synapses on spines, dendritic trunks, and cell bodies in area 17 of the cat. *J Comp Neurol*. 231:180–189.

Biederer T, Kaeser PS, Blanpied TA. 2017. Transcellular nanoalignment of synaptic function. *Neuron*. 96:680–696.

Blazquez-Llorca L, Merchán-Pérez Á, Rodríguez JR, Gascón J, DeFelipe J. 2013. FIB/SEM technology and AD: three-dimensional analysis of human cortical synapses. *J Alzheimers Dis*. 34:995–1013.

Blazquez-Llorca L, Woodruff A, Inan M, Anderson SA, Yuste R, DeFelipe J, Merchán-Pérez Á. 2015. Spatial distribution of neurons innervated by chandelier cells. *Brain Struct Funct*. 220:2817–2834.

Bourne JN, Harris KM. 2011. Coordination of size and number of excitatory and inhibitory synapses results in a balanced structural plasticity along mature hippocampal CA1 dendrites during LTP. *Hippocampus*. 21:354–373.

Braak H, Braak E. 1992. The human entorhinal cortex: normal morphology and lamina-specific pathology in various diseases. *Neurosci Res*. 15:6–31.

Cohen NJ, Squire LR. 1980. Preserved learning and retention of pattern-analyzing skill in amnesia: dissociation of knowing how and knowing that. *Science*. 210:207–210.

Colonnier M. 1968. Synaptic patterns on different cell types in the different laminae of the cat visual cortex. An electron microscope study. *Brain Res*. 9:268–287.

DeFelipe J. 1997. Types of neurons, synaptic connections and chemical characteristics of cells immunoreactive for calbindin-D28K, parvalbumin and calretinin in the neocortex. *J Chem Neuroanat*. 14:1–19.

DeFelipe J. 2002. Cortical interneurons: from Cajal to 2001. *Prog Brain Res*. 136:215–238.

DeFelipe J. 2011. The evolution of the brain, the human nature of cortical circuits and intellectual creativity. *Front Neuroanat*. 5:29.

DeFelipe J. 2015. The anatomical problem posed by brain complexity and size: a potential solution. *Front Neuroanat*. 9:104.

DeFelipe J, Fariñas I. 1992. The pyramidal neuron of the cerebral cortex: morphological and chemical characteristics of the synaptic inputs. *Prog Neurobiol*. 39:563–607.

DeFelipe J, Fairén A. 1993. A simple and reliable method for correlative light and electron microscopic studies. *J Histochem Cytochem*. 41:769–772.

DeFelipe J, Fernández-Gil MA, Kastanauskaite A, Palacios Bote R, Gañán Presmanes Y, Trinidad Ruiz M. 2007. Macroanatomy and microanatomy of the temporal lobe. *Semin Ultrasound CT MRI*. 28:404–415.

Domínguez-Álvaro M, Montero-Crespo M, Blazquez-Llorca L, DeFelipe J, Alonso-Nanclares L. 2019. 3D electron microscopy study of synaptic Organization of the Normal Human Transentorhinal Cortex and its possible alterations in Alzheimer's disease. *eNeuro*. 6:1–17.

Domínguez-Álvaro M, Montero-Crespo M, Blazquez-Llorca L, Insausti R, DeFelipe J, Alonso-Nanclares L. 2018. Three-dimensional analysis of synapses in the transentorhinal cortex of Alzheimer's disease patients. *Acta Neuropathol Commun*. 6:20.

Duvernoy HM. 2005. *The human hippocampus: functional anatomy, vascularization and serial sections with MRI*. 3rd ed. Berlin, Heidelberg, New York: Springer-Verlag.

Freund TF, Buzsáki G. 1996. Interneurons of the hippocampus. *Hippocampus*. 6:347–470.

Freund TF, Katona I. 2007. Perisomatic inhibition. *Neuron*. 56:33–42.

Froemke RC. 2015. Plasticity of cortical excitatory-inhibitory balance. *Annu Rev Neurosci*. 8:195–219.

Ganeshina O, Berry RW, Petralia RS, Nicholson DA, Geinisman Y. 2004a. Differences in the expression of AMPA and NMDA receptors between axospinous perforated and nonperforated synapses are related to the configuration and size of postsynaptic densities. *J Comp Neurol*. 468: 86–95.

Ganeshina O, Berry RW, Petralia RS, Nicholson DA, Geinisman Y. 2004b. Synapses with a segmented, completely partitioned postsynaptic density express more AMPA receptors than other axospinous synaptic junctions. *Neuroscience*. 125:615–623.

Geinisman Y, Morrell F, DeToledo-Morrell L. 1987. Axospinous synapses with segmented postsynaptic densities: a morphologically distinct synaptic subtype contributing to the number of profiles of 'perforated' synapses visualized in random sections. *Brain Res*. 423:179–188.

Gomez-Isla T, Price JL, McKeel DW, Morris JC, Growdon JH, Hyman BT. 1996. Profound loss of layer II entorhinal cortex neurons occurs in very mild Alzheimer's disease. *J Neurosci*. 16:4491–4500.

Gray EG. 1959. Axo-somatic and axo-dendritic synapses of the cerebral cortex: an electron microscope study. *J Anat*. 4:420–433.

Gundersen HJG, Bendtsen TF, Korbo L, Marcussen N, Miziller A, Nielsen K, Nyengaard JR, Pakkenberg B, Sørensen FB, Vesterby A *et al*. 1988. Some new, simple and efficient stereological methods and their use in pathological research and diagnosis. *APMIS*. 96:379–394.

Holderith N, Lorincz A, Katona G, Rózsa B, Kulik A, Watanabe M, Nusser Z. 2012. Release probability of hippocampal glutamatergic terminals scales with the size of the active zone. *Nat Neurosci*. 15:988–997.

Houser CR, Vaughn JE, Hendry SHC, Jones EG, Peters A. 1984. GABA neurons in the cerebral cortex. In: Jones EG, Peters A, editors. *Cerebral cortex. Vol. 2. functional properties of cortical cells*. New York: Plenum Press, pp. 63–89.

Ino T, Matsuzaki S, Shinonaga Y, Ohishi H, Ogawa-Meguro R, Mizuno N. 1990. Direct projections of non-pyramidal neurons of Ammon's horn to the amygdala and the entorhinal cortex. *Neurosci Lett*. 115:161–166.

Insausti R, Amaral DG. 2012. Hippocampal Formation. In: Mai JK, Paxinos G, editors. *The human nervous system*. Academic Press, pp. 896–Cambridge (MA), 942.

Insausti R, Muñoz-López M, Insausti AM, Artacho-Pérula E. 2017. The human Periallocortex: layer pattern in presubiculum, parasubiculum and entorhinal cortex. A review. *Front Neuroanat*. 11:84.

Jones DG, Calverley RK. 1991. Perforated and non-perforated synapses in rat neocortex: three-dimensional reconstruction. *Brain Res*. 556:247–258.

Kobro-Flatmoen A, Witter MP. 2019. Neuronal chemoarchitecture of the entorhinal cortex: a comparative review. *Eur J Neurosci*. 50:3627–3662.

Kondo H, Lavenex P, Amaral DG. 2009. Intrinsic connections of the macaque monkey hippocampal formation: II. CA3 connections. *J Comp Neurol*. 515:349–377.

Kumar SS, Buckmaster PS. 2006. Hyperexcitability, interneurons, and loss of GABAergic synapses in entorhinal cortex in a model of temporal lobe epilepsy. *J Neurosci*. 26:4613–4623.

Lavenex P, Amaral DG. 2000. Hippocampal-neocortical interaction: a hierarchy of associativity. *Hippocampus*. 10: 420–430.

Markram H, Muller E, Ramaswamy S, Reimann MW, Abdellah M, Sanchez CA, Ailamaki A, Alonso-Nanclares L, Antille N, Arsever S *et al*. 2015. Reconstruction and simulation of neocortical microcircuitry. *Cell*. 163:456–492.

Megías M, Emri Z, Freund TF, Gulyás AI. 2001. Total number and distribution of inhibitory and excitatory synapses on hippocampal CA1 pyramidal cells. *Neuroscience*. 102:527–540.

Melzer S, Michael M, Caputi A, Eliava M, Fuchs EC, Whittington MA, Monyer H. 2012. Long-range-projecting GABAergic neurons modulate inhibition in hippocampus and entorhinal cortex. *Science*. 335:1506–1510.

Merchán-Pérez A, Rodríguez JR, Alonso-Nanclares L, Schertel A, DeFelipe J. 2009. Counting synapses using FIB/SEM microscopy: a true revolution for ultrastructural volume reconstruction. *Front Neuroanat*. 3:18.

Merchán-Pérez A, Rodríguez JR, González S, Robles V, DeFelipe J, Larrañaga P, Bielza C. 2014. Three-dimensional spatial distribution of synapses in the neocortex: a dual-beam electron microscopy study. *Cereb Cortex*. 24:1579–1588.

Montero-Crespo M, Domínguez-Álvaro M, Rondón-Carrillo P, Alonso-Nanclares L, DeFelipe J, Blazquez-Llorca L. 2020. Three-dimensional synaptic organization of the human hippocampal CA1 field. *Elife*. 9:e57013.

Morales J, Alonso-Nanclares L, Rodríguez JR, DeFelipe J, Rodríguez Á, Merchán-Pérez Á. 2011. Espina: a tool for the automated segmentation and counting of synapses in large stacks of electron microscopy images. *Front Neuroanat*. 18:18.

Morales J, Rodríguez A, Rodríguez JR, DeFelipe J, Merchan-Pérez A. 2013. Characterization and extraction of the synaptic apposition surface for synaptic geometric analysis. *Front Neuroanat*. 7:20.

Neuman KM, Molina-Campos E, Musial TF, Price AL, Oh KJ, Wolke ML, Buss EW, Scheff SW, Mufson EJ, Nicholson DA. 2015. Evidence for Alzheimer's disease-linked synapse loss and compensation in mouse and human hippocampal CA1 pyramidal neurons. *Brain Struct Funct*. 220:3143–3165.

Nusser Z, Hájos N, Somogyi P, Mody I. 1998. Increased number of synaptic GABAA receptors underlies potentiation at hippocampal inhibitory synapses. *Nature*. 395:172–177.

Oorschot D, Peterson D, Jones D. 1991. Neurite growth from, and neuronal survival within, cultured explants of the nervous system: a critical review of morphometric and stereological methods, and suggestions for the future. *Prog Neurobiol*. 37:525–546.

Peters A. 1987. *Synaptic specificity in the cerebral cortex*. In: Edelman GM, Gall WE, Cowan WM editors. Synaptic Function. New York: John Wiley, p. 373–397.

Peters A, Palay SL, Webster HD. 1991. *The fine structure of the nervous system. Neurons and their supporting cells*. New York: Oxford University Press.

Peters A, Palay SL. 1996. The morphology of synapses. *J Neurocytol*. 25:687–700.

Ribak CE. 1978. Aspinous and sparsely-spinous stellate neurons in the visual cortex of rats contain glutamic acid decarboxylase. *J Neurocytol*. 7:461–478.

Santuy A, Rodríguez J, DeFelipe J, Merchán-Pérez A. 2018a. Study of the size and shape of synapses in the juvenile rat somatosensory cortex with 3D. *Electron Microscopy eNeuro*. 5:1–14.

Santuy A, Rodriguez JR, DeFelipe J, Merchán-Pérez A. 2018b. Volume electron microscopy of the distribution of synapses in the neuropil of the juvenile rat somatosensory cortex. *Brain Struct Funct*. 223:77–90.

Scheff SW, Sparks DL, Price DA. 1993. Quantitative assessment of synaptic density in the entorhinal cortex in Alzheimer's disease. *Ann Neurol*. 34:356–361.

Schubert D, Kötter R, Staiger JF. 2007. Mapping functional connectivity in barrel-related columns reveals layer- and cell type-specific microcircuits. *Brain Struct Funct*. 212:107–119.

Schultz H, Sommer T, Peters J. 2015. The role of the human Entorhinal cortex in a representational account of memory. *Front Hum Neurosci*. 9.

Sohal VS, Rubenstein JLR. 2019. Excitation-inhibition balance as a framework for investigating mechanisms in neuropsychiatric disorders. *Mol Psychiatry*. 24:1248–1257.

Solodkin A, Van Hoesen GW. 1996. Entorhinal cortex modules of the human brain. *J Comp Neurol*. 365:610–617.

Somogyi P, Tamás G, Lujan R, Buhl EH. 1998. Salient features of synaptic organisation in the cerebral cortex. *Brain Res Brain Res Rev*. 26:113–135.

Spruston N. 2008. Pyramidal neurons: dendritic structure and synaptic integration. *Nat Rev Neurosci*. 9:206–222.

Südhof TC. 2012. The presynaptic active zone. *Neuron*. 75:11–25.

Takumi Y, Ramirez-Leon V, Laake P, Rinvik E, Ottersen OP. 1999. Different modes of expression of AMPA and NMDA receptors in hippocampal synapses. *Nat Neurosci*. 2: 618–624.

Tarusawa E, Matsui K, Budisantoso T, Molnar E, Watanabe M, Matsui M, Fukazawa Y, Shigemoto R. 2009. Input-specific intrasynaptic arrangements of ionotropic glutamate receptors and their impact on postsynaptic responses. *J Neurosci*. 29:12896–12908.

Tremblay R, Lee S, Rudy B. 2016. GABAergic interneurons in the Neocortex: from cellular properties to circuits. *Neuron*. 91:260–292.

Van Hoesen GW, Hyman BT, Damasio AR. 1991. Entorhinal cortex pathology in AD. *Hippocampus*. 1:1–8.

Vicent-Lamarre P, Lynn M, Béïque JC. 2018. The eloquent silent synapse. *Trends Neurosci*. 41:557–559.

White EL. 1989. *Cortical circuits: synaptic organization of the cerebral cortex. structure, function and theory*. Boston: Birkhäuser.

Witter MP, Doan TP, Jacobsen B, Nilssen ES, Ohara S. 2017. Architecture of the entorhinal cortex a review of Entorhinal anatomy in rodents with some comparative notes. *Front Syst Neurosci*. 11:46.

Wouterlood FG, Pothuizen H. 2000. Sparse colocalization of somatostatin- and GABA-immunoreactivity in the entorhinal cortex of the rat. *Hippocampus*. 10:77–86.

Wouterlood FG, Hartig W, Bruckner G, Witter MP. 1995. Parvalbumin-immunoreactive neurons in the entorhinal cortex of the rat: localization, morphology, connectivity and ultrastructure. *J Neurocytol*. 24:135–153.

Yakoubi R, Rollenhagen A, von Lehe M, Miller D, Walkenfort B, Hasenberg M, Sätzler K, JHR L *et al*. 2019a. Ultrastructural heterogeneity of layer 4 excitatory synaptic boutons in the adult human temporal lobe neocortex. *Elife*. 20:e48373.

Yakoubi R, Rollenhagen A, von Lehe M, Shao Y, Sätzler K, Lübke JHR. 2019b. Quantitative three-dimensional reconstructions of excitatory synaptic Boutons in layer 5 of the adult human temporal lobe Neocortex: a fine-scale electron microscopic analysis. *Cereb Cortex*. 29:2797–2814.

Zhou S, Yu Y. 2018. Synaptic E-I balance underlies efficient neural coding. *Front Neurosci*. 12:46.